



ORIGINAL PAPER

Amin Moosaie · Ali Sharifian

Numerical simulation of steady incompressible slip flow around a circular cylinder at low Reynolds numbers

Received: 18 February 2024 / Revised: 29 June 2024 / Accepted: 13 August 2024
© The Author(s), under exclusive licence to Springer-Verlag GmbH Austria, part of Springer Nature 2024

Abstract Steady viscous flow past a circular cylinder with velocity slip boundary condition is numerically solved. The Navier–Stokes equations are solved using the vorticity-stream function formulation for two-dimensional incompressible flows. A time-accurate solver is developed which can be used for accurate solution of time-dependent flows. However, only steady results for Reynolds numbers up to 40 are presented in this paper. Most of the emphasis is dedicated to the validation of the solver and the results, something which is more or less missing in previous studies of slip flows. There has been a controversy regarding the computation of the drag coefficient and its various contributions in the past. As reviewed in the text, some papers did not present the formulation of the drag coefficient and only presented the results, some papers used the no-slip formulae and some papers presented formulae for the slip case but did not validate them. Due to this controversy, we derived formulae for the various contributions to the drag coefficient and validated them by comparison to existing data, especially using an analytical solution of Oseen’s equation for creeping flow around a cylinder with slip condition. At the end, some results are presented including wall vorticity and slip velocity distribution, streamlines, vorticity contours and various contributions to the drag coefficient.

1 Introduction

Flow about bluff bodies such as a circular cylinder has a paramount importance in technical applications as well as fundamental studies of fluid mechanics. Such flows exhibit distinct features such as flow separation, vortex shedding in the near and far fields, fluctuations in lift and drag forces, etc. Hence, there has been a great deal of research dedicated to study various aspects of this problem by analytical, numerical and experimental means [1]. Another interesting yet complicated feature of the flow past curved surfaces is a variable separation point which is dictated, not only by the obstacle geometry, but also by the dynamics of the oncoming flow [2]. This is essentially different from the flow separation on a cube where the point of separation is solely determined by sharp edges of the obstacle [3].

Flow around a circular cylinder is an outstanding benchmark problem to study bluff body aerodynamics, see for example [4–6]. This flow exhibits different regimes depending on the Reynolds number based on the cylinder diameter, denoted by Re . For the interval $0 < Re \leq 6$, we observe no separation and hence no recirculation zone. Steady flow separation can be seen in the range of $6 < Re \leq 47$, where a symmetric pair of vortices exist right behind the cylinder. Unsteady effects and periodic vortex shedding is observed in the range $48 < Re \leq 160$. Aperiodic flow separation starts to take place from about $Re = 160$ and it gradually shows three-dimensional effects and instabilities which lead to transition in the wake. Of course, the aforementioned limits of intervals are just approximate values and they stand for the no-slip case. In the present work, we study the steady flow regime around a cylinder with wall velocity slip. In a systematic investigation of the

A. Moosaie (✉) · A. Sharifian
Turbulence Research Laboratory, Department of Mechanical Engineering, Yasouj University, 75914-353 Yasouj, Iran
E-mail: moosaie@yu.ac.ir

flow around a circular cylinder, the above regimes are being studied. The present paper addresses the steady separated flow regime under the influence of wall slip. The unsteady regime will remain to be the subject of subsequent investigations.

Slip flow on solid walls is encountered in a number of situations such as flow of water over hydrophobic [7] and superhydrophobic [8] surfaces, and the boundary-layer flows of rarefied gases provided that the degree of rarefaction is up to the limit where it can still be described by means of continuum theories [9]. For such flows, the amount of wall slip is determined by a dimensionless group called the Knudsen number, which quantifies the degree of rarefaction of the gas. The Knudsen number based on the cylinder diameter is denoted by Kn throughout this paper. In this context, $Kn = 0$ implies the classical no-slip condition, i.e. zero tangential velocity on the wall, whereas $Kn \rightarrow \infty$ gives the full slip condition, i.e. zero shear stress on the wall. There exist various formulations of wall slip boundary condition. In the present work, we use the classical Maxwell's slip model [10].

Increasing the wall slip in a laminar boundary layer leads to a decreased overall drag, thinner boundary layer thickness, delayed transition to turbulence, increased heat transfer without the temperature jump at the wall, and decreased heat transfer even below the no-slip values when the temperature jump is taken into account [11, 12]. An analytical solution of the Oseen's equation for creeping flow, i.e. low Reynolds number flow, around a cylinder shows that the total drag coefficient decreases by increasing the amount of wall slip [13]. This behavior has been verified to exist for moderate Reynolds numbers [14]. Although it was conceived that the vorticity generation at the wall is due to the no-slip condition, it is now well known that vorticity can be generated at the wall, even at full slip (zero wall shear stress) [15]. Leal [15] also showed that although the wall slip deteriorates the vorticity generation at the wall, it somehow enhances the vorticity convection in the downstream direction after its generation.

The effect of variable slip length on the flow over a cylinder has been investigated numerically [16]. They have used the commercial software FLUENT to perform the simulations. Although they did not mention how the drag coefficient is computed, they have validated their computed drag coefficient against an approximate analytical solution based on the solution of Proudman and Pearson [17]. However, their validation is only for the total drag coefficient and they did not discuss the various contributions to the drag in their validation.

The slip flow around the cylinder is simulated by Seo and Song [18], by solving the shallow water equations instead of the full Navier–Stokes equations. They did not give the formulation used for the calculation of the drag coefficient. However, the formula they gave for the pressure distribution on the cylinder surface in terms of the wall vorticity is the one of no-slip flows.

Maghsoudi et al. [19] numerically solved the steady laminar flow and heat transfer around a circular cylinder using a stream function-vorticity formulation. They have used no-slip formulae to compute the pressure and viscous drag coefficient.

Minimum power consumption for drag reduction in the slip flow around a cylinder was studied using analytical and numerical means [20]. Although the drag coefficient was studied, they only wrote the drag force as the integral of viscous and pressure forces exerted by the flow on the cylinder, similar to the integral shown in Eq. (18). However, explicit formulae for the computation of drag coefficient were not given.

Transient flows around slippery circular and elliptic cylinders are respectively simulated in [21, 22], using a stream function-vorticity formulation. Formulae for drag and lift coefficients are given and start-up of the flow is investigated. No validation of the formulae for drag and lift coefficients is provided. However, an asymptotic solution is obtained which is valid for a short time interval at the flow start-up. This is used to validate the velocity field.

The two- and three-dimensional unsteady flow and heat transfer around a circular cylinder with wall slip was simulated by Rehman et al. [23]. They focused on the Nusselt number and they did not give formulae and diagrams showing the drag coefficient.

Due to discrepancy in the data presented and since there has been no thorough and extensive validation of the simulation results presented for slip flow around a circular cylinder, the main objective of the present paper is the validation of this canonical flow setup by using the existing data. Moreover, as there exist a controversy on how to compute the drag coefficient in such flows, as discussed above, another aim is to eradicate this controversy by proposing formulae, derived from the first principles, to compute various contributions to the drag coefficient and validate it against the existing analytical data of Atefi [13].

2 Problem setup

An infinitely long circular cylinder of radius R is subjected to a cross flow of a constant-properties rarefied gas with undisturbed velocity U_∞ . This flow configuration is schematically depicted in Fig. 1. The free flow Mach number $\text{Ma}_\infty = U_\infty/c_\infty$ is small enough so that the incompressible flow assumption holds valid, with c_∞ being the speed of sound at the free flow condition. Therefore, the gas density ρ , dynamic viscosity μ and kinematic viscosity $\nu = \mu/\rho$ are assumed constant. The outer boundary of the computational domain is a sufficiently large circle of radius R_{out} , non-dimensionally written as $R_\infty = R_{\text{out}}/R$.

Unless otherwise stated, all quantities in this paper are non-dimensionalized by the cylinder radius R , the free-stream velocity U_∞ and the free-stream pressure p_∞ . Also, the Reynolds number based on the cylinder diameter is defined as $\text{Re} = 2RU_\infty/\nu$.

3 Theory and governing equations

3.1 Equations of motion

With the assumptions made in Sect. 2, the flow is governed by the time-dependent, two-dimensional and incompressible continuity and Navier–Stokes equations, written in their dimensionless form as

$$\nabla \cdot \mathbf{u} = 0, \quad (1)$$

$$\frac{\partial \mathbf{u}}{\partial t} + (\mathbf{u} \cdot \nabla) \mathbf{u} = -\nabla p + \frac{2}{\text{Re}} \Delta \mathbf{u}, \quad (2)$$

where \mathbf{u} , p , ∇ and Δ are the velocity vector, the pressure, the nabla operator and the Laplacian operator, respectively.

Due to the incompressibility and two-dimensionality of the flow, the stream function-vorticity formulation of the Navier–Stokes equations is used. In what follows, the equations are written in the cylindrical coordinate system, in which u_r and u_θ are the radial and circumferential velocity components, respectively. The stream function ψ is related to velocity components via

$$u_r = \frac{1}{r} \frac{\partial \psi}{\partial \theta}, \quad u_\theta = -\frac{\partial \psi}{\partial r}. \quad (3)$$

The vorticity ω is related to the velocity components and the stream function respectively via

$$\omega = \frac{1}{r} \left[\frac{\partial(r u_\theta)}{\partial r} - \frac{\partial u_r}{\partial \theta} \right], \quad (4)$$

$$\omega = -\frac{1}{r} \frac{\partial}{\partial r} \left(r \frac{\partial \psi}{\partial r} \right) - \frac{1}{r^2} \frac{\partial^2 \psi}{\partial \theta^2}. \quad (5)$$

Equation (5) is a Poisson equation for the stream function ψ . The vorticity transport equation reads

$$\frac{\partial \omega}{\partial t} + \frac{1}{r} \frac{\partial \psi}{\partial \theta} \frac{\partial \omega}{\partial r} - \frac{1}{r} \frac{\partial \psi}{\partial r} \frac{\partial \omega}{\partial \theta} = \frac{2}{\text{Re}} \left(\frac{\partial^2 \omega}{\partial r^2} + \frac{1}{r} \frac{\partial \omega}{\partial r} + \frac{1}{r^2} \frac{\partial^2 \omega}{\partial \theta^2} \right). \quad (6)$$

Equations (5) and (6) constitute a set of two nonlinear partial differential equations which can be solved to obtain the vorticity and stream function. Once the stream function is computed, the velocity components are obtained using Eq. (3). This approach is equivalent to solving the Navier–Stokes equations (2) for two-dimensional incompressible flow problems, since the solution will indentially satisfy the continuity Eq (1).

The boundary conditions are as follows. On the cylinder surface, i.e. at $r = 1$, we have

$$\psi(r = 1, \theta, t) = 0, \quad \left. \frac{\partial^2 \psi}{\partial r^2} \right|_{r=1} = \alpha \left. \frac{\partial \psi}{\partial r} \right|_{r=1}. \quad (7)$$

Note that the first condition ensures that the cylinder surface is indeed a flow streamline, i.e. the surface is impervious with $u_r(r = 1, \theta, t) = 0$. The second one applies the Navier's velocity slip condition on the cylinder surface [10, 13], in which α is defined by

$$\alpha = \frac{\sigma}{2(2 - \sigma)} \frac{1}{\text{Kn}} + 1, \quad (8)$$

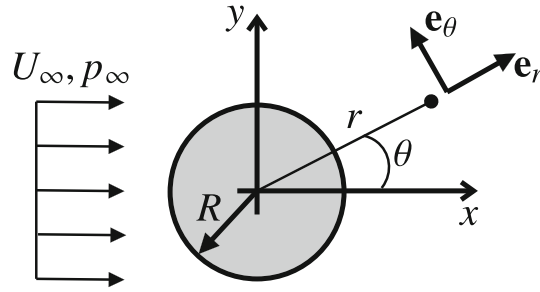


Fig. 1 The problem geometry, parameters, the cylindrical coordinate system and the unit base vectors in radial and circumferential directions

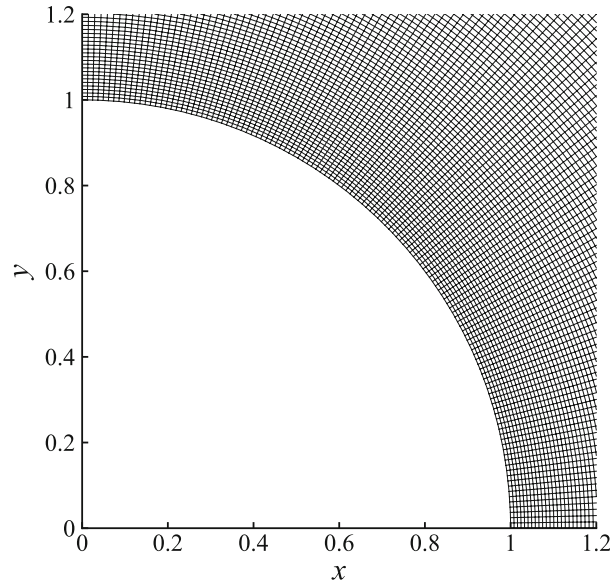


Fig. 2 The computational grid of 512^2 grid points in the physical space. Only one quarter in the vicinity of the cylinder is shown

where σ is the tangential momentum accommodation coefficient. For an extremely rough wall at the molecular level, which pertains to virtually all practical applications of macroscopic scale, one can assume that $\sigma = 1$. From the definition (8), it is obvious that $\alpha \in [1, \infty)$, $\alpha = 1$ describes the full slip (zero wall shear stress) condition while $\alpha \rightarrow \infty$ describes the classical no-slip condition. Moreover, Kn is the Knudsen number based on the cylinder diameter $2R$, defined by

$$\text{Kn} = \frac{\lambda}{2R}, \quad (9)$$

with λ being the molecular mean free path of the gas. For a dilute gas consisting of a single chemical species, λ is given by

$$\lambda = \frac{k_B T}{\sqrt{2} \pi d^2 p}, \quad (10)$$

in which k_B , T , d and p are the Boltzmann constant, the gas absolute temperature, the effective diameter of the gas molecules and the gas pressure, respectively. We also need a boundary condition at the cylinder surface relating the vorticity to the stream function. This can be obtained from Eqs. (5) and (7):

$$\omega(r = 1, \theta, t) = -\frac{1 + \alpha}{\alpha} \frac{\partial^2 \psi}{\partial r^2} \Big|_{r=1}. \quad (11)$$

Table 1 Coefficients of frictional, pressure and total drag, and also the separation angle for $Re = 10$ and $Kn = 0$, obtained by using 128^2 , 256^2 , 512^2 and 700^2 grid points, and $R_\infty = 80$.

Grid	C_{DF}	C_{DP}	C_D	θ_{sep} (deg.)
128^2	1.2338	1.5798	2.8136	27.12
256^2	1.2337	1.5814	2.8151	28.27
512^2	1.2337	1.5819	2.8156	28.82
700^2	1.2336	1.5822	2.8158	28.86
Correlations (33)	1.2244	1.5706	2.7550	28.71
S. & B. [26]	1.231	1.600	2.831	28.73

Comparison is made with correlations and numerical results of [26,27]

Table 2 Coefficients of frictional, pressure and total drag, and also the separation angle for $Re = 10$ and $Kn = 0$, obtained by using 512^2 grid points and domain sizes of $R_\infty = 40, 60, 80$ and 100

R_∞	C_{DF}	C_{DP}	C_D	θ_{sep} (deg.)
40	1.2656	1.6294	2.8950	29.02
60	1.2437	1.5968	2.8405	28.92
80	1.2337	1.5819	2.8156	28.82
100	1.2333	1.5815	2.8148	28.79

At far distance $r = R_\infty$, a potential flow is assumed and thus

$$\psi(r = R_\infty, \theta, t) = \left(R_\infty - \frac{1}{R_\infty}\right) \sin \theta, \quad \omega(r = R_\infty, \theta, t) = 0. \quad (12)$$

Since an unsteady solution is performed, initial conditions need to be supplied as well. In all the simulations reported in this paper, a potential flow is taken for the initialization of ψ and ω , i.e.

$$\psi(r, \theta, t = 0) = \left(r - \frac{1}{r}\right) \sin \theta, \quad \omega(r, \theta, t = 0) = 0. \quad (13)$$

In practice, the second initial condition is only required and the initial ψ is computed by solving the Poisson Eq. (5).

In order to have a stretched mesh in the radial direction which accounts for the near-wall sharp gradients, the radial direction r of the physical space is transformed into a computational space, called z , via $r = e^z$ or $z = \ln r$. This is equivalent to using the conformal mapping $z + i\theta = \ln(x + iy)$, with x and y being the Cartesian coordinates. This constitutes an orthogonal curvilinear grid. The so-obtained grid used for the computations is shown in Fig. 2. With this transform, all first and second derivatives with respect to r must be calculated with respect to z by using the chain rule of differentiation. By applying this transform, Eqs. (5) and (6) read

$$\frac{\partial^2 \psi}{\partial z^2} + \frac{\partial^2 \psi}{\partial \theta^2} = -e^{2z} \omega(z, \theta, t), \quad (14)$$

$$\frac{\partial \omega}{\partial t} = e^{-2z} \left[\frac{\partial \psi}{\partial z} \frac{\partial \omega}{\partial \theta} - \frac{\partial \psi}{\partial \theta} \frac{\partial \omega}{\partial z} + \frac{2}{Re} \left(\frac{\partial^2 \omega}{\partial z^2} + \frac{\partial^2 \omega}{\partial \theta^2} \right) \right], \quad (15)$$

Since $z = 0$ at the cylinder surface, all the derivatives with respect to r at $r = 1$ equal to their corresponding derivatives with respect to z at $z = 0$. This is used in the application of wall boundary conditions.

Once ψ and ω fields are computed, all other flow quantities can be obtained by post-processing. The velocity components are computed by simply differentiating ψ , according to Eq. (3). The calculation of the pressure distribution on the cylinder surface is presented in the appendix §A whereas the drag and lift coefficients are defined in §3.2.

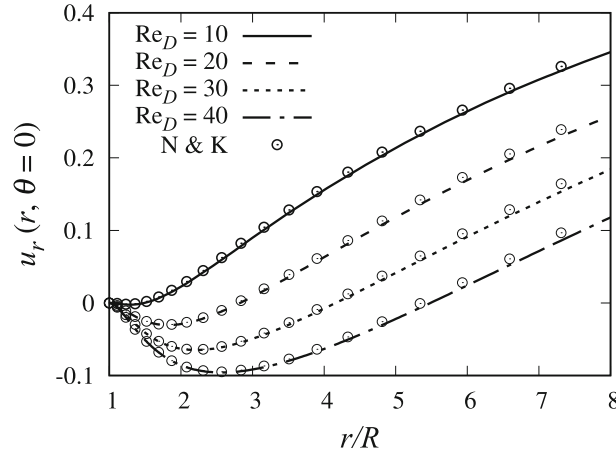


Fig. 3 The centerline radial velocity $u_r(r, \theta = 0)$ for $\text{Kn} = 0$ (no-slip) and $\text{Re} = 10, 20, 30$ and 40 compared with the results of Nieuwstadt and Keller [28]

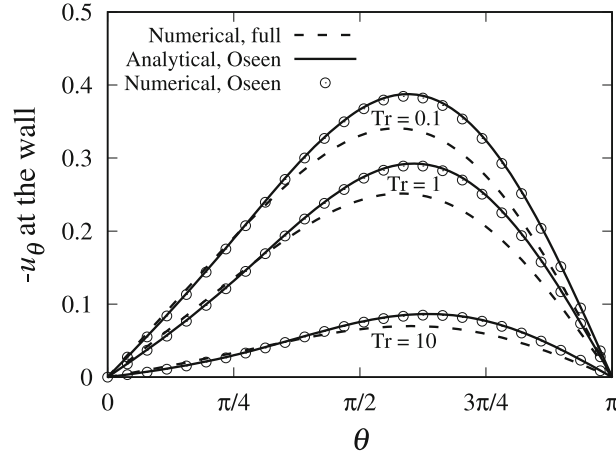


Fig. 4 Slip velocity as a function of the circumferential angle θ at $\text{Re} = 1$ for $\text{Tr} = 0.1, 1$ and 10 . The analytical [13] and the numerical solutions of Oseen's equation are plotted as well. For the numerical solution of Oseen's equation, every fifth point is plotted

3.2 Drag coefficient

The pressure C_{DP} , frictional C_{DF} and total drag coefficients are important quantities in aerodynamics. For the classical no-slip condition, it is well known that these quantities are computed by

$$C_{DP} = -\frac{2}{\text{Re}} \int_0^{2\pi} \left(\frac{\partial \omega}{\partial r} \right)_{r=1} \sin \theta \, d\theta. \quad (16a)$$

$$C_{DF} = +\frac{2}{\text{Re}} \int_0^{2\pi} \omega|_{r=1} \sin \theta \, d\theta, \quad (16b)$$

The total drag coefficient C_D is then computed by summing up C_{DP} and C_{DF} :

$$C_D = C_{DP} + C_{DF}. \quad (16c)$$

For the wall slip condition, various approaches have been devised so far. Seo and Song [18] and Maghsoudi et al. [19] used no-slip formulae (16) for the slip flow around a circular cylinder. D'Alessio [21] derived the following relation for the total drag coefficient for the slip flow over a circular cylinder, see also [22] for the

Table 3 Coefficients of frictional, pressure and total drag, and the separation angle for $Re = 20$ and 40 , and $Kn = 0$ using 512^2 grid points and $R_\infty = 80$, compared with correlations and numerical results of [14,26,27]

Re	Data source	C_{DF}	C_{DP}	C_D	θ_{sep} (deg.)
20	Present work	0.8075	1.2257	2.0332	43.24
	Sucker and Brauer [26]	0.853	1.325	2.178	42.80
	Legendre et al. [14]	–	–	2.045	–
	Correlations (33)	0.8023	1.2168	2.0243	43.33
40	Present work	0.5229	0.9949	1.5178	53.23
	Sucker and Brauer [26]	0.557	1.076	1.633	51.94
	Sen et al. [27]	–	–	1.5093	–
	Correlations (33)	0.5239	0.9897	1.5075	53.61

proof using the conformal mapping method.

$$C_D = \frac{2}{Re} \int_0^{2\pi} \left(\frac{\partial \omega}{\partial r} - \omega \right) \Big|_{r=1} \sin \theta \, d\theta + \frac{\beta^2}{2(1+\beta)^2} \int_0^{2\pi} \omega^2 \Big|_{r=1} \cos \theta \, d\theta - \int_0^{2\pi} \frac{\partial u_\theta}{\partial t} \Big|_{r=1} \sin \theta \, d\theta, \quad (17)$$

where β is defined as the slip coefficient appearing in the slip condition formulated in the computational space, i.e. $u_\theta = \beta \partial u_\theta / \partial z$ [21]. However, he does not give explicit formulae for different contributions to the total drag coefficient. The signs in Eq. (17) are different from those of Eq. (16) due to the fact that the free-stream flow is in negative x -direction in [21] whereas it is in positive x -direction in the present work.

None of the above-mentioned formulae have been validated against analytical and/or experimental data for the slip flow case. Here, we derive equations for all contributions to the total drag coefficients for the slip flow around a circular cylinder from the first principles, and validate them by comparison with an available analytical solution of Oseen's equation [13].

The drag coefficient C_D is calculated by integrating the horizontal component of the dimensionless pressure and viscous (normal and shear) stresses over the cylinder surface:

$$C_D = - \int_0^{2\pi} \left(-p_w + \frac{4}{Re} \frac{\partial u_r}{\partial r} \right) \Big|_{r=1} \cos \theta \, d\theta + \frac{2}{Re} \int_0^{2\pi} \left(\frac{\partial u_\theta}{\partial r} - \frac{u_\theta}{r} \right) \Big|_{r=1} \sin \theta \, d\theta, \quad (18)$$

In order to calculate $\partial u_r / \partial r$ appeared in the first integral of Eq. (18), we start from the continuity equation in cylindrical coordinates, which yields $(\partial u_r / \partial r)_{r=1} = -(\partial u_\theta / \partial \theta)_{r=1}$. Now, by employing the slip boundary condition

$$\left[\frac{\partial u_\theta}{\partial r} - \alpha u_\theta \right]_{r=1} = 0, \quad (19)$$

and the definition of vorticity (4), one can write

$$\left[\frac{\partial u_r}{\partial r} \right]_{r=1} = - \left[\frac{\partial u_\theta}{\partial \theta} \right]_{r=1} = - \frac{1}{\alpha + 1} \left[\frac{\partial \omega}{\partial \theta} \right]_{r=1}. \quad (20)$$

It shall be noted here that the contribution from the viscous normal stress $4/Re (\partial u_r / \partial r)$ to the drag only exists in the slip flows and it vanishes in no-slip flows for obvious reasons.

By the help of the slip boundary condition (19), the shear strain-rate at the cylinder surface appeared in the second integral of Eq. (18) can be written in terms of the vorticity at the wall:

$$\left[\frac{\partial u_\theta}{\partial r} - \frac{u_\theta}{r} \right]_{r=1} = \frac{\alpha - 1}{\alpha + 1} \omega \Big|_{r=1}. \quad (21)$$

The wall pressure appeared in the first integral of equation (18) is also provided by Eq. (45) (see appendix §A). Now, we have all the elements required to calculate the drag coefficients. The so-obtained drag coefficient reads

$$C_D = C_{D1} + C_{D2} + C_{D3} + C_{D4} + C_{D5}, \quad (22a)$$

Table 4 Drag coefficient contributions $C_{DP} = C_{D1} + C_{D2} + C_{D3}, C_{D4}, C_{D5}$ and the total drag coefficient C_D for $Re = 1$ and, $Tr = 0.1, 1, 10$ and ∞ , with $Tr = \alpha - 1 = 1/(2Kn)$, obtained by the numerical solution of the full Navier–Stokes as well as Oseen’s equations, compared with the results of an analytical solution of Oseen’s equation [13]

Tr	Data source	C_{DP}	C_{D4}	C_{D5}	C_D
0 (full slip)	Present, N-S, Eq. (22)	4.4799	4.3556	0.0	8.8355
	Present, N-S, Eq. (17)	4.4799	4.3816		8.8615
	S. & A. [20], N-S	—	—	—	9.01
	Present, Oseen, Eq. (22)	4.9735	4.7792	0.0	9.7528
	Present, Oseen, Eq. (17)	4.9735	4.8031		9.7767
0.1	Analytical [13], Oseen	4.8773	4.7701	0.0	9.6474
	Present, N-S, Eq. (22)	4.5179	4.1833	0.2104	8.9117
	Present, N-S, Eq. (17)	4.5179	4.4185		8.9364
	Present, Oseen, Eq. (22)	5.0190	4.5959	0.2309	9.8459
	Present, Oseen, Eq. (17)	5.0190	4.8495		9.8685
1	Analytical [13], Oseen	4.9199	4.5850	0.2293	9.7341
	Present, N-S, Eq. (22)	4.7270	3.0645	1.5409	9.3324
	Present, N-S, Eq. (17)	4.7270	4.6226		9.3496
	Present, Oseen, Eq. (22)	5.2774	3.3989	1.7070	10.3832
	Present, Oseen, Eq. (17)	5.2774	5.1209		10.3983
10	Analytical [13], Oseen	5.1902	3.3989	1.6994	10.2885
	Present, N-S, Eq. (22)	5.1244	0.8319	4.1798	10.1361
	Present, N-S, Eq. (17)	5.1244	5.0158		10.1402
	Present, Oseen, Eq. (22)	5.7348	0.9413	4.7203	11.3964
	Present, Oseen, Eq. (17)	5.7348	5.6644		11.3992
∞ (no-slip)	Analytical [13], Oseen	5.7302	0.9489	4.7443	11.4234
	Present, N-S, Eq. (22)	5.2711	1.03E-5	5.1640	10.4351
	Present, N-S, Eq. (17)	5.2711	5.1640		10.4351
	S. & A. [20], N-S	—	—	—	10.64
	S. & B. [26], N-S	5.355	—	5.225	10.570
	Present, Oseen, Eq. (22)	5.8642	1.17E-5	5.8633	11.7275
	Present, Oseen, Eq. (17)	5.8641	5.8633		11.7274
	Analytical [13], Oseen	5.9284	1.19E-4	5.9283	11.8569

Drag coefficients formulae (17) [21] and (22) are compared. For results obtained using Eq. (17), only $C_{DF} = C_{D4} + C_{D5}$ is available. For all the simulations at $Re = 1$, $R_\infty = 600$ is chosen. Comparison with the numerical results of [20] for the full slip case and with those of [20,26] for the no-slip case is presented

Table 5 Total drag coefficient with full slip condition ($Kn \rightarrow \infty$) for $Re = 5, 20, 50, 100$ and 200 , using 512^2 grid points and $R_\infty = 80$ ($R_\infty = 120$ for $Re = 5$), compared with numerical results of Legendre et al. [14]

Re	Data source	C_D
5	Present work	3.1637
	Legendre et al. [14]	3.15
20	Present work	1.3285
	Legendre et al. [14]	1.33
50	Present work	0.7125
	Legendre et al. [14]	0.712
100	Present work	0.4154
	Legendre et al. [14]	0.415
200	Present work	0.2299
	Legendre et al. [14]	0.228

in which

$$C_{D1} = -\frac{2}{Re} \int_0^{2\pi} \left. \frac{\partial \omega}{\partial r} \right|_{r=1} \sin \theta \, d\theta, \quad (22b)$$

$$C_{D2} = -\frac{1}{2(\alpha + 1)^2} \int_0^{2\pi} \left. \omega^2 \right|_{r=1} \cos \theta \, d\theta, \quad (22c)$$

$$C_{D3} = \int_0^{2\pi} \left. \frac{\partial u_\theta}{\partial t} \right|_{r=1} \sin \theta \, d\theta, \quad (22d)$$

$$C_{D4} = \frac{4}{\text{Re}} \frac{1}{\alpha + 1} \int_0^{2\pi} \left. \frac{\partial \omega}{\partial \theta} \right|_{r=1} \cos \theta \, d\theta, \quad (22e)$$

$$C_{D5} = \frac{2}{\text{Re}} \frac{\alpha - 1}{\alpha + 1} \int_0^{2\pi} \omega|_{r=1} \sin \theta \, d\theta. \quad (22f)$$

The first integral of Eq. (18) produces the contributions C_{D1} to C_{D4} whereas the second integral produces C_{D5} . While the pressure drag consists of C_{D1} to C_{D3} , C_{D4} is the viscous drag produced by the viscous normal stress (i.e. the second term in the first integral of Eq. (18) which is only non-zero in slip flows and it vanishes in no-slip flows) and C_{D5} is the viscous drag produced by the viscous shear stress. C_{D3} is not considered in the present work as we study the steady-state flow.

Due to the fact that $(\alpha + 1)u_\theta = \omega$ at $r = 1$, C_{D3} can be rephrased in terms of the vorticity:

$$C_{D3} = \frac{1}{\alpha + 1} \int_0^{2\pi} \left. \frac{\partial \omega}{\partial t} \right|_{r=1} \sin \theta \, d\theta. \quad (23)$$

Moreover, if we perform an integration by parts in Eq. (22e), we get

$$C_{D4} = \frac{4}{\text{Re}} \frac{1}{\alpha + 1} \int_0^{2\pi} \omega|_{r=1} \sin \theta \, d\theta. \quad (24)$$

Adding C_{D4} given in Eq. (24) to C_{D5} given in Eq. (22f) yields

$$C_{D4} + C_{D5} = \frac{2}{\text{Re}} \int_0^{2\pi} \omega|_{r=1} \sin \theta \, d\theta \quad (25)$$

With this modification, Eq. (22) becomes similar to the drag coefficient formula (17) given by [21] for slippery flow around a circular cylinder. However, we prefer to separately calculate C_{D4} and C_{D5} using Eqs. (22e) and (22f) rather than combining them as shown in Eq. (25) which is equivalent to using formulation (17) given in [21]. Because, although the sum of contributions C_{D4} and C_{D5} is similar to the no-slip formula (26b), it does not tell us how the viscous drag is generated. The more detailed contributions C_{D4} and C_{D5} show that by increasing wall slip, the contribution from the viscous normal stress C_{D4} increases while that of the viscous shear stress C_{D5} decreases. That also explains how we do have viscous drag even at full slip $\alpha = 1$.

It is worthwhile to mention that, in steady flows, it is possible to compute the total drag coefficient by the no-slip formulae (22a) plus the C_{D2} contribution given in Eq. (22c). It means that in papers where C_D of the slip flow is computed by simply using the no-slip formula (22a), e.g. see [18, 19], the C_{D2} contribution to the pressure drag has been ignored. The significance of this contribution will be discussed in the sequel.

Because of the coordinate transform $r = e^z$ used in this paper, all the evaluations at $r = 1$ must be done at $z = 0$. Also, $\partial\omega/\partial r$ at $r = 1$ in Eq. (22b) must be replaced with $\partial\omega/\partial z$ at $z = 0$.

Finally, we can decompose the drag coefficient to pressure C_{DP} and frictional C_{DF} contributions similar to what is conventionally done for the no-slip condition. In this manner, we have

$$C_{DP} = C_{D1} + C_{D2} + C_{D3}, \quad (26a)$$

$$C_{DF} = C_{D4} + C_{D5}. \quad (26b)$$

It is worthwhile to note that the contribution C_{D4} is classified as part of the pressure drag in [13]. But, since C_{D4} arises from the viscous normal stress, we believe that it is more suitable to be included in the frictional drag. At the no-slip limit when $\alpha \rightarrow \infty$, the above drag coefficient reduces to the well-known no-slip results (16).

4 Numerical methods

A numerical solution strategy is developed here which is accurate at each time step so that the unsteady flow phenomena can be resolved with high accuracy and efficiency, though we use it in this paper to obtain steady-state solution. In contrast to steady solvers which solve the Poisson equation for the stream function only once, a time-accurate solver requires a fully converged solution of the Poisson equation at each time step. This can be a very demanding task in terms of computation time. Therefore, a very efficient method is used in this work for the solution of the Poisson equation, which will be explained in the sequel.

All flow quantities are periodic in the circumferential direction θ with a period of 2π . Due to the periodicity and the use of uniform grid in the circumferential direction, we use the fast Fourier transform (FFT) technique in this direction, and thus, the Poisson equation (14) reads

$$\frac{d^2 \hat{\psi}}{dz^2} - k'^2 \hat{\psi}(z, k, t) = -e^{2zi} \hat{\omega}(z, k, t), \quad (27)$$

where $\hat{\psi}$ and $\hat{\omega}$ are respectively the Fourier-transform of ψ and ω . Also, k' is the modified wavenumber of the second-order central difference scheme (CDS2) for the second derivative, i.e. $k'^2 = 2 [1 - \cos(k\Delta\theta)] / \Delta\theta^2$ with $\Delta\theta$ being the grid spacing in the θ -direction and k being the FFT wavenumber [24]. Equation (27) is an ordinary differential equation (ODE) in the z -direction for each modified wavenumber k' . Thus, for all wavenumbers, it constitutes a set of ODEs. The discretization of the derivative with respect to z in Eq. (27) is done by the CDS2 scheme:

$$\frac{\hat{\psi}_{i+1,j}^n - 2\hat{\psi}_{i,j}^n + \hat{\psi}_{i-1,j}^n}{\Delta z^2} - k'^2 \hat{\psi}_{i,j}^n = -e^{2zi} \hat{\omega}_{i,j}^n, \quad (28)$$

where i and j are respectively the spatial grid indices in the z and θ directions, and n is the time step counter. The boundary conditions must be Fourier-transformed as well:

$$\hat{\psi}_{1,j}^n = 0, \quad \hat{\psi}_{n_z,j}^n = \text{FFT} \left\{ \left(R_\infty - \frac{1}{R_\infty} \right) \sin \theta \right\}, \quad (29)$$

where n_z is the index of the last grid point in the z -direction.

Equation (28) defines a complex tridiagonal system of linear algebraic equations for each modified wavenumber k' and at each time step n . A complex version of the tridiagonal matrix algorithm (TDMA), called CTDMA, is used for a very efficient and fast solution of these systems. The application of the CTDMA gives the stream function in the Fourier space. Then, a simple application of the inverse fast Fourier transform (IFFT) technique results in the desired stream function ψ in the physical space. This algorithm yields a direct and efficient solution of the Poisson Eq. (14) up to the machine accuracy at each time step. The FORTRAN library FFTW3 is used in the present work to perform the required forward and backward FFTs.

In Eq. (15), the first and second derivatives of the stream function and the vorticity with respect to z and θ are discretized using CDS2, e.g.

$$\left. \frac{\partial \psi}{\partial z} \right|_{i,j}^n = \frac{\psi_{i+1,j}^n - \psi_{i-1,j}^n}{2\Delta z} + O(\Delta z^2), \quad (30a)$$

$$\left. \frac{\partial^2 \psi}{\partial z^2} \right|_{i,j}^n = \frac{\psi_{i+1,j}^n - 2\psi_{i,j}^n + \psi_{i-1,j}^n}{\Delta z^2} + O(\Delta z^2). \quad (30b)$$

Similar formulae are used for the derivatives with respect to θ and for the derivatives of the vorticity field ω . The boundary conditions are also treated by CDS2 schemes, as will be explained in Sect. 4.1. Since all the constituents of the numerical method are CDS2, the entire scheme is formally second-order accurate in space. CDS2 is used in all spatial discretizations to avoid numerical viscosity through upwinding whatsoever.

The time stepping is done by an explicit, low-storage, third-order Runge–Kutta scheme [25]. Equation (15) is a nonlinear advection–diffusion equation for which, the above-explained numerical method is conditionally stable. The time step size for each run is taken such that the simulation is stable.

4.1 Boundary closures at the wall

The wall boundary closures are obtained by enforcing a discretized version of wall boundary conditions in the following manner. Boundary condition (11) is discretized by using the CDS2:

$$\omega_{1,j}^n = -\frac{1+\alpha}{\alpha} \frac{\psi_{2,j}^n - 2\psi_{1,j}^n + \psi_{0,j}^n}{\Delta z^2} + O(\Delta z^2), \quad (31)$$

in which $\psi_{0,j}^n$ is not inside the computational domain and it is computed using a CDS2 discretized version of the second condition in Eq. (7):

$$\frac{\psi_{2,j}^n - 2\psi_{1,j}^n + \psi_{0,j}^n}{\Delta z^2} = \alpha \frac{\psi_{2,j}^n - \psi_{0,j}^n}{2\Delta z} + O(\Delta z^2). \quad (32a)$$

Rearrangement of Eq. (32a) yields

$$\psi_{0,j}^n = \frac{2}{2 + \alpha\Delta z} \left[2\psi_{1,j}^n + \left(\frac{\alpha\Delta z}{2} - 1 \right) \psi_{2,j}^n \right] + O(\Delta z^2). \quad (32b)$$

5 Code validation and convergence

The numerical methods presented in the previous section have been implemented as a FORTRANcode. In this section, we present the validation of the numerical algorithm and the verification of its computer implementation. For this purpose, we first illustrate the independence of the results upon the grid resolution and the domain size R_∞ . Next, a comparison with an available analytical solution based on Oseen's equation for the creeping flow, i.e. flow at very small Reynolds numbers, around a circular cylinder with wall slip condition [13] is supplied. This validates the steady-state solution. In order to check the accuracy of the unsteady solver, the wall vorticity is validated against an asymptotic analytical solution [21] which is approximately valid for relatively large Reynolds numbers and short times after the flow onset. It means that the validation is done for both low and high Reynolds numbers and both steady and unsteady flows.

Table 1 shows the coefficients of frictional, pressure and total drag, and also the separation angle for $Re = 10$ and $Kn = 0$, i.e. no-slip condition, obtained by using 128^2 , 256^2 , 512^2 and 1024^2 number of grid points. In these simulations, the domain size, normalized by the cylinder radius, was taken as a constant to be $R_\infty = 80$. It is observed that the friction, pressure and total drag coefficients and the separation angle are respectively within 0.016%, 0.15%, 0.078% and 6.029% relative error, comparing the results of the coarsest mesh with those of the finest mesh. These are acceptable results for grid convergence and Table 1 shows that a 256^2 grid is already sufficient to resolve the significant flow physics. However, to be on the safe side and to guarantee the accuracy and grid independence of the results, unless otherwise stated, we used 512^2 grids for all the simulations presented in this paper.

In order to investigate the effect of the computational domain size, we have run simulations with four domain sizes, i.e. $R_\infty = 40, 60, 80$ and 100 . The results for the coefficients of frictional, pressure and total drag as well as the separation angle are given in Table 2. In all simulations, the grid resolution was kept constant and chosen to be 512^2 . It turns out that the relative error in the frictional, pressure and total drag are 1.91%, 2.19% and 2.06%, respectively. The separation angles predicted by the two simulations are indistinguishable. Again, to be on the safe side, we used a domain of size $R_\infty = 80$ in all the simulations presented in this paper. The only exceptions are the very low Reynolds number flows, as it was shown in [26] that a larger computational domain is needed for such flows. Thus, we used $R_\infty = 120$ for $Re = 5$, and $R_\infty = 600$ for creeping flow simulations at $Re = 1$ for both Navier-Stokes and Oseen solvers, see the following paragraphs concerning the creeping flow solver based on Oseen's hydrodynamic equation. It is notable that Maghsoudi et al. [19] used $R_\infty = 20$ for their simulations.

Table 3 shows the frictional, pressure and total drag coefficients as well as the separation angle at $Re = 10, 20$ and 40 for $Kn = 0$ (no-slip case) of the present simulation and results of [26]. In order to have comparison with some recent publications, the C_D of [14] at $Re = 20$ and of [27] at $Re = 40$ are also given. The following correlations for the drag coefficients [27] and the separation angle [26] in the no-slip case are also used for comparison:

$$C_{DF} = -0.016 + 4.938 Re^{-0.60}, \quad \text{for } 6 \leq Re \leq 40, \quad (33a)$$

$$C_{DP} = 0.583 + 4.311 Re^{-0.64}, \quad \text{for } 6 \leq Re \leq 40, \quad (33b)$$

$$C_D = 0.26 + 7.89 Re^{-0.5}, \quad \text{for } 15 \leq Re \leq 40, \quad (33c)$$

$$\theta_{sep} = \left(\frac{\ln(Re) - 1.83}{3 \times 10^{-4}} \right)^{0.456}, \quad \text{for } 6.23 \leq Re \leq 1000. \quad (33d)$$

The above validations made for the drag coefficient which is an integrated quantity. In order to check the accuracy of the code in more details, e.g. in terms of the velocity field, the radial velocity profiles along the x -axis, i.e. $u_\theta(r, \theta = 0)$, of the no-slip flow at various Reynolds numbers are plotted in Fig. 3 and compared with

the data of Nieuwstadt and Keller [28]. The agreement is excellent near the cylinder and it slightly deteriorates by increasing the distance from the cylinder. The slight discrepancy far from the cylinder might be attributed to the relatively low resolution and the smaller domain size used in [28], dictated by limited computational resources in 1973.

So far, the no-slip results are validated against existing data. It means that all parts of the solver are validated, except for the part that applies the slip boundary condition and the part that computes the drag coefficient based on (22). As mentioned in the literature study, there are not much publications on slip flow over a cylinder. Moreover to this, most of the existing publications do not mention how they computed the drag coefficient. Some of the authors, e.g. [19] even used the no-slip formula (16) to compute C_D in a slip flow. Therefore, one could say that the formulae for drag coefficient of the cylinder in a slip flow have not yet been rigorously validated. In order to do this, we use an existing analytical solution, as explained below.

Atefi [13] has obtained an analytical solution of the Oseen's equation for creeping flow around a circular cylinder with slip boundary condition. In his work, the circumferential velocity field is given by

$$u_\theta(r, \theta) = -\left(1 + \frac{1}{r^2}\right) \sin \theta + \frac{1}{4} \sum_{m=0}^{\infty} \sum_{n=1}^{\infty} B_m \left[\frac{F_{m,n}(k)}{r^{n+1}} - P_{m,n}(kr) \right] \sin n\theta, \quad (34a)$$

where $k = \text{Re}/4$ and the auxiliary functions $F_{m,n}$ and $P_{m,n}$ are given by

$$F_{m,n} = K_m (I_{m+n-1} + I_{m-n+1} + I_{m-n-1} + I_{m+n+1}) + (K_{m-1} + K_{m+1}) (I_{m-n} + I_{m+n}), \quad (34b)$$

$$P_{m,n} = K_m (I_{m-n-1} - I_{m-n+1} - I_{m+n-1} + I_{m+n+1}) + (K_{m+1} - K_{m-1}) (I_{m-n} - I_{m+n}), \quad (34c)$$

with I_m and K_m being the m th-order modified Bessel function of the first and second kind, respectively. The constants B_m in Eq. (34a) are calculated by solving a linear set of algebraic Equations [13]. In [13], the wall slip is quantified by a dimensionless group called the Trostel number (denoted by Tr) which is related to the Knudsen number and our slip parameter α via

$$\text{Tr} = \frac{\sigma}{2(2 - \sigma)} \frac{1}{\text{Kn}} = \alpha - 1. \quad (35)$$

In order to obtain the required data for the comparison, the above analytical solution has been programmed by the first author and the data have been re-computed, of course with the correction made by Moosaie [29] to the definition of $P_{m,n}$ in Eq. (34c). Figure 4 shows the circumferential velocity u_θ at the wall, i.e. the fluid slip velocity at the wall, as a function of the angle θ for $\text{Re} = 1$ and, $\text{Tr} = 0.1, 1$ and 10 . The agreement is generally good, but not perfect. At the first glance, we were not sure whether the discrepancy is due to a mistake in the algorithm/code or it is due to the fact that Atefi's results are from the solution of Oseen's equation and our results are from the solution of Navier–Stokes equation. Though, we conjectured that the latter be the case. To check whether this is true, the Oseen's equation in the vorticity-stream function formulation is numerically solved using our solver. The vorticity Eq. (15) is substituted by its Oseen's approximation [30]:

$$\frac{\partial \omega}{\partial t} = e^{-2z} \left[\cosh z \sin \theta \frac{\partial \omega}{\partial \theta} - \sinh z \cos \theta \frac{\partial \omega}{\partial z} + \frac{2}{\text{Re}} \left(\frac{\partial^2 \omega}{\partial z^2} + \frac{\partial^2 \omega}{\partial \theta^2} \right) \right]. \quad (36)$$

By a rapid comparison of Eqs. (15) and (36), it is obvious that the only changes we have to make in our numerical code is the substitution of $\partial \psi / \partial z$ with $\cosh z \sin \theta$ and $\partial \psi / \partial \theta$ with $\sinh z \cos \theta$. All the other parts of the code remain unchanged. Thus, this benchmark is a very good validation of the code. Equation (36) is independent of ψ and it is only written in terms of ω . But, the boundary conditions, which are the same as the full Navier–Stokes problem, require the stream function. As a post-processing also, the stream function is needed to compute the velocity components and to draw the streamlines. Thus, the Poisson equation for ψ , i.e. Eq. (14), is simultaneously solved. The results of the so-obtained numerical solution of Oseen's flow are plotted in Fig. 4 as well. The excellent agreement between the analytical and numerical results for the Oseen's equation reassures that the algorithm and its computer implementation, specifically the slip boundary condition, are programmed correctly.

Moreover, the results of the total drag coefficient for the same case ($\text{Re} = 1$) are shown in Table 4 and compared with those of the analytical solution. We observe that the analytical values of C_D are in general smaller than those of the simulation, within about 10% difference. It is worthwhile to mention that C_D predicted numerically in [26] for $\text{Re} = 1$ and $\text{Tr} \rightarrow \infty$ is 10.57, which is in very good agreement with our numerical

result. Also, Fig. 8b of reference [13] shows that in the range $1 \leq \text{Re} \leq 10$, the Oseen's theory overestimates the drag coefficient as compared to the solution of full Navier–Stokes equations for the no-slip case. This behavior is verified by our simulation as shown in Table 4 for the slip case. For comparison, we computed the drag coefficients using both D'Alessio's formulation (17) and the proposed formula (22). We observe that D'Alessio's formula slightly overestimates C_D as compared to formula (22). Furthermore, if we change the definition of C_{D3} from (22e) to (24), the results of both formulations coincide (not presented here). This coincidence is expected as we theoretically proved in §3.2 that the two formulations collapse to one with the use of Eqs. (24) and (25).

The total drag coefficient data for full slip condition, i.e. $\text{Kn} \rightarrow \infty$, are given in [14]. Our results are compared with those of [14] in Table 5 at $\text{Re} = 5, 20, 50, 100$ and 200. An excellent agreement is observed.

Although steady-state results are only presented in this paper, but in order to check the accuracy of the developed unsteady solver for the study of time-dependent flow fields, we use an asymptotic analytical solution of the wall vorticity for the flow around a circular cylinder with slip boundary condition [21]. This solution is valid for large Reynolds numbers and short times after the flow start-up. The wall vorticity ω_0 is given by

$$\omega_0(\theta, t) = \frac{2(1 + \beta)}{\beta} \left(1 - \frac{(1 + \beta)\Lambda}{\sqrt{\pi}\beta} \right) \sin \theta, \quad (37)$$

where $\Lambda = \sqrt{8t/\text{Re}}$ (λ in [21]) and D'Alessio's slip parameter β is related to our slip parameter α via $\beta = 1/\alpha$. It shows that the wall vorticity has a sinusoidal behavior around the cylinder surface. Figure 5 represents the wall vorticity ω_0 as a function of θ at $\text{Re} = 1000$ for $\beta = 1.0$ and $t = 0.5$. An excellent agreement is observed between the numerical and the analytical velocity profiles. The very small discrepancy is attributed to the approximate nature of the asymptotic analytical solution (37). The results for other values of β and Λ are in good agreement as well, and hence are not shown here for the sake of brevity.

6 Results and discussions

In this section, the simulation results for steady flow around the cylinder with wall slip are presented. Simulations were conducted for $\text{Re} = 5, 10, 15, 20, 25, 30, 35$ and 40. For the full slip flow with $\text{Kn} \rightarrow \infty$, also simulations at $\text{Re} = 50, 100$ and 200 were conducted in order to compare the total drag coefficient with the results of Legendre et al. [14]. At each Reynolds number, we considered cases with $\text{Kn} = 0, 0.001, 0.005, 0.01, 0.03$ and 0.05. Some flow streamlines, the separation angle, the length of the separation bubble and the drag coefficient are studied. Specifically, various contributions to the drag coefficient are studied in detail.

The flow streamlines and vorticity contours at $\text{Re} = 10$ and 20 are plotted in Fig. 6 for $\text{Kn} = 0$ (no-slip) and 0.05. It is observed that by increasing the Knudsen number at constant Reynolds number, the length of the recirculation zone and the separation angle decrease. A similar trend is observed at other Reynolds numbers that are computed but they are not shown.

The behavior of the separation angle by changing Knudsen number is best observed in Fig. 7, where the separation angle (in degrees) is plotted versus the Knudsen number for various Reynolds numbers. We see that, at a given Re , the separation angle is almost a linear function of Kn . On the other hand, Fig. 8 shows the separation angle (in degrees) versus the Reynolds number for various Knudsen numbers. The trends are similar for various Knudsen numbers, but the functionality is not linear anymore. The smaller separation angle at smaller Kn can be attributed to the higher tangential momentum of the fluid elements adjacent to the wall at larger slip, i.e. at smaller Kn . The fluid elements with higher tangential momentum can better overcome the adverse pressure gradient and go on further downstream before being separated.

The length of the separation bubble in the range of steady flow, i.e. approximately $\text{Re} < 50$, is plotted in Fig. 9 versus Knudsen number, for various Reynolds numbers. Similar to the separation angle, a linear dependence of the bubble length upon Knudsen number is observed. The lines of various Reynolds numbers are almost parallel to each other. As expected, a decreasing behavior of the bubble length by increasing Knudsen number at a given Reynolds number is observed. The bubble length as a function of Reynolds number is plotted in Fig. 10 for various Knudsen numbers. Unlike the separation angle, the behavior is somewhat linear. But, the lines are not parallel and their slope increases by decreasing Knudsen number.

The vorticity distribution along the cylinder wall is plotted in Fig. 11 for various Knudsen numbers at $\text{Re} = 10, 20, 30$ and 40. It is observed that up to about $\pi/2$, the wall vorticity increases by increasing Knudsen number. After about $\pi/2$, the behavior is somewhat different and the wall vorticity decreases by increasing Knudsen number. The angle at which the behavior changes increases by increasing Reynolds number. The

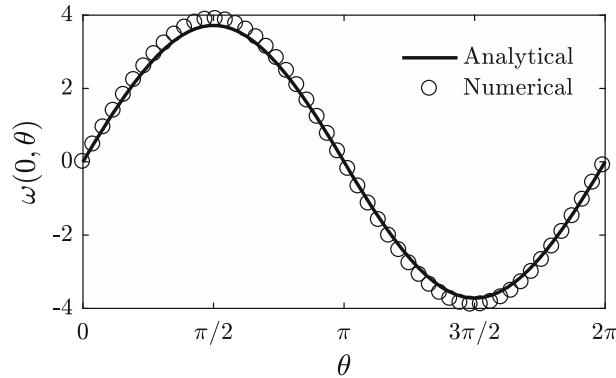


Fig. 5 Wall vorticity as a function of the circumferential angle θ at $Re = 1000$ for $\beta = 1.0$ and $t = 0.5$. For the numerical results, every fifth point is plotted. The analytical solution is taken from [21]

peaks of maximum wall vorticity increase by increasing Reynolds number while it decreases by increasing Knudsen number. It is straightforward to show from the slip boundary condition (19) that the following relation holds at the wall:

$$\omega = -\left(\frac{1}{2Kn} + 2\right)u_{\theta}. \quad (38)$$

This right-hand side of Eq. (38) is plotted in Fig. 11a as well and the satisfaction of Eq. (38) is checked.

The slip velocity, i.e. the circumferential velocity at the wall, is plotted in Fig. 12 for various Knudsen numbers at $Re = 10, 20, 30$ and 40 . For the no-slip case with $Kn = 0$, the slip velocity is zero everywhere as expected. For higher Knudsen numbers, a negative region of u_{θ} is observed which corresponds to the separation zone. The negative region increases in magnitude and span by increasing Reynolds number, but decreases by increasing Knudsen number. The peak of u_{θ} at the wall increases by increasing both Reynolds and Knudsen numbers.

The radial velocity gradient $\partial u_r / \partial r$ is important in the contribution of the viscous normal stress to the drag coefficient, i.e. C_{D4} . Figure 13 plots the quantity $\partial u_r / \partial r$ versus angle for various Knudsen numbers at $Re = 20$. It is observed that this contribution vanishes for classical no-slip flows, that is why people do not consider this contribution to the drag coefficient when dealing with no-slip flows. However, by increasing Knudsen numbers, this term becomes more and more important and this contribution can not be neglected anymore. Figure 14 shows the same quantity versus angle for various Reynolds numbers at $Kn = 0.05$. We see that for this slip Knudsen number, this contribution does never vanish and it gets stronger by increasing Reynolds number.

The contributions C_{D1} , C_{D2} , C_{D4} and C_{D5} along with the total drag coefficient C_D are plotted in Fig. 15 versus Knudsen number at $Re = 10, 20, 30$ and 40 . First of all, we observe a linear dependence of all drag contributions as well as the total drag upon Knudsen number. C_{D1} remains almost constant within the range of Knudsen numbers considered. However, it shows slight changes in a complicated manner. By increasing Kn , C_{D1} slightly decreases at $Re = 10$ and 20 whereas it slightly increases at $Re = 30$ and 40 . The C_{D2} contribution is zero at $Kn = 0$ and is negative for higher Knudsen numbers. Its magnitude slightly increases by increasing Kn . At higher Knudsen numbers, not shown here, it becomes more and more significant. It means that in papers where the authors used the no-slip formulae (16) to compute the drag coefficient, the contribution of C_{D2} is neglected and therefore, their results for the drag coefficient become more and more inaccurate by increasing Kn . C_{D4} , which is zero for the no-slip case, gradually increases by increasing Kn . C_{D5} is maximum for no-slip flow and it decreases by increasing Knudsen number. The total drag coefficient C_D is also maximum for no-slip flow and it decreases by increasing Kn . As discussed theoretically, the results confirm that the viscous normal stress contribution C_{D4} increases by increasing Kn while the viscous shear stress contribution C_{D5} decreases.

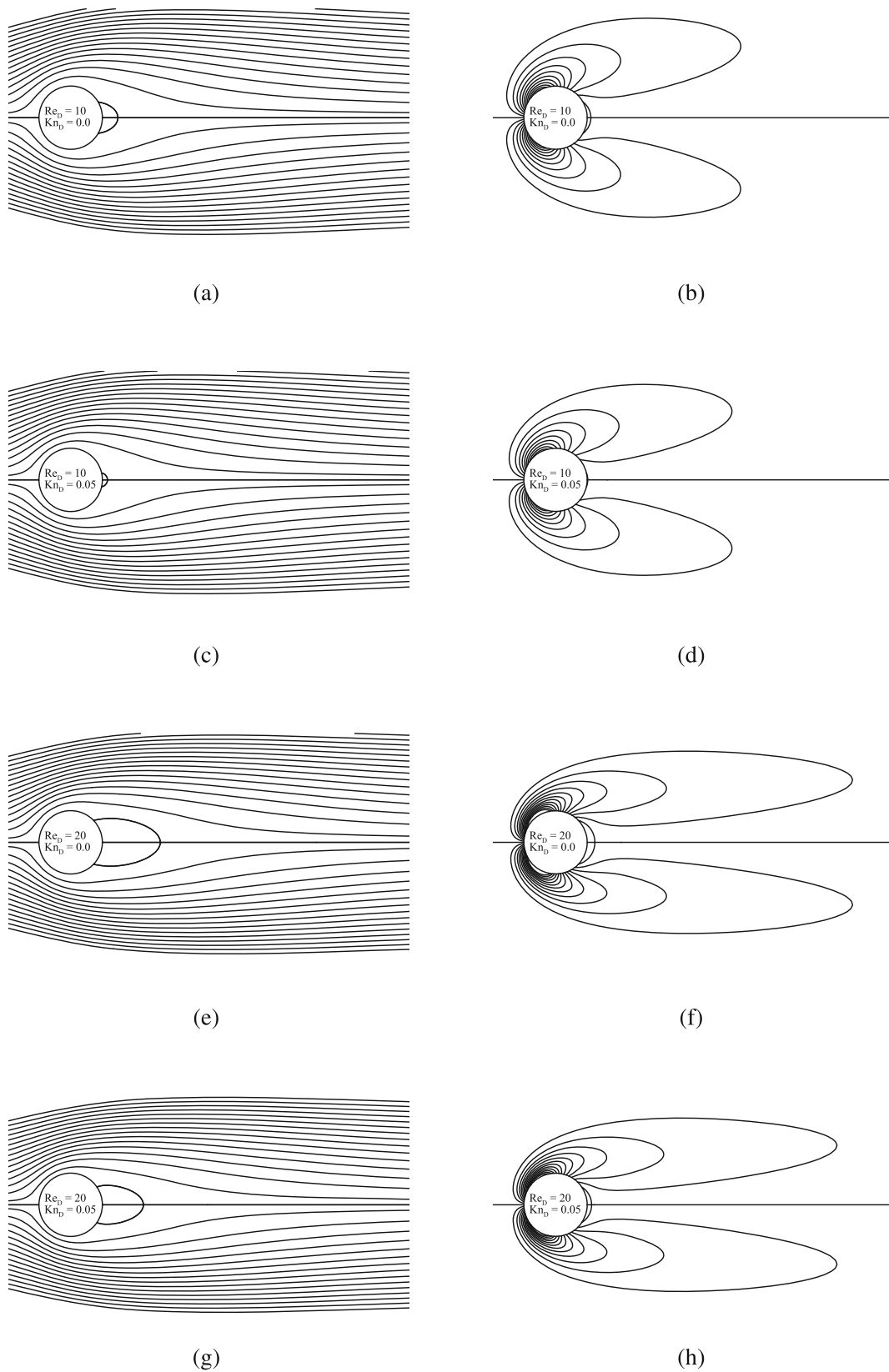


Fig. 6 The flow streamlines (left) and the vorticity field (right) around the cylinder at $Re = 10$ and 20 , and $Kn = 0$ and 0.05

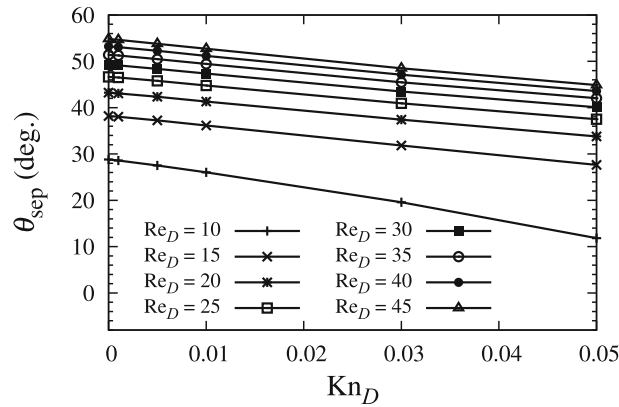


Fig. 7 The separation angle in the steady flow regime versus Kn for various values of Re

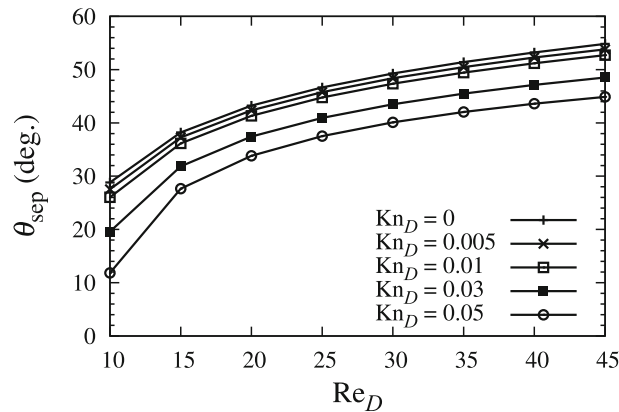


Fig. 8 The separation angle in the steady flow regime versus Re for $Kn = 0, 0.005, 0.01, 0.03$ and 0.05 . The case $Kn = 0.001$ is not shown as its results almost coincide with those of $Kn = 0$

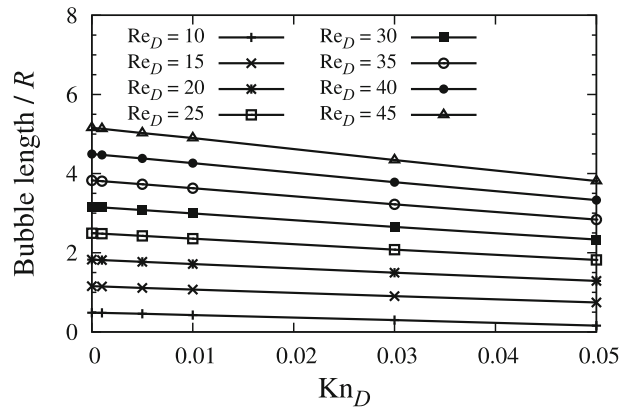


Fig. 9 The length of the separation bubble in the steady flow regime versus Kn for various values of Re

7 Conclusions

Steady viscous slip flow around a circular cylinder is numerically investigated. The flow is simulated using the vorticity-stream function formulation of Navier–Stokes equations for two-dimensional incompressible flows. A time-accurate solver is developed which can be used for accurate solution of time-dependent flows. Nevertheless, only steady flow case is presented in this paper. Most of the emphasis is dedicated to the validation of the solver and the results, something which is more or less missing in previous studies. There has been a controversy regarding the computation of the drag coefficient and its various contributions in the past. As

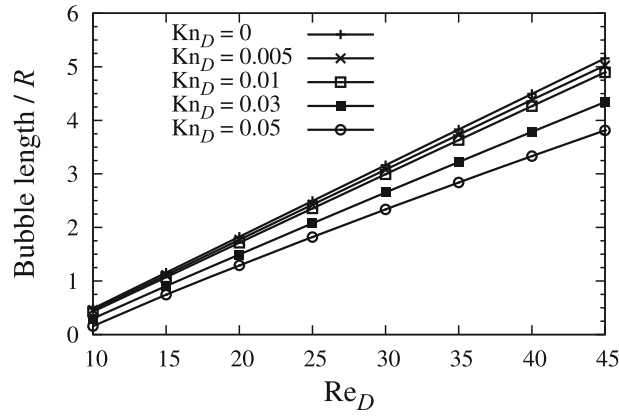


Fig. 10 The length of the separation bubble in the steady flow regime versus Re for $Kn = 0, 0.005, 0.01, 0.03$ and 0.05 . The case $Kn = 0.001$ is not shown as its results almost coincide with those of $Kn = 0$

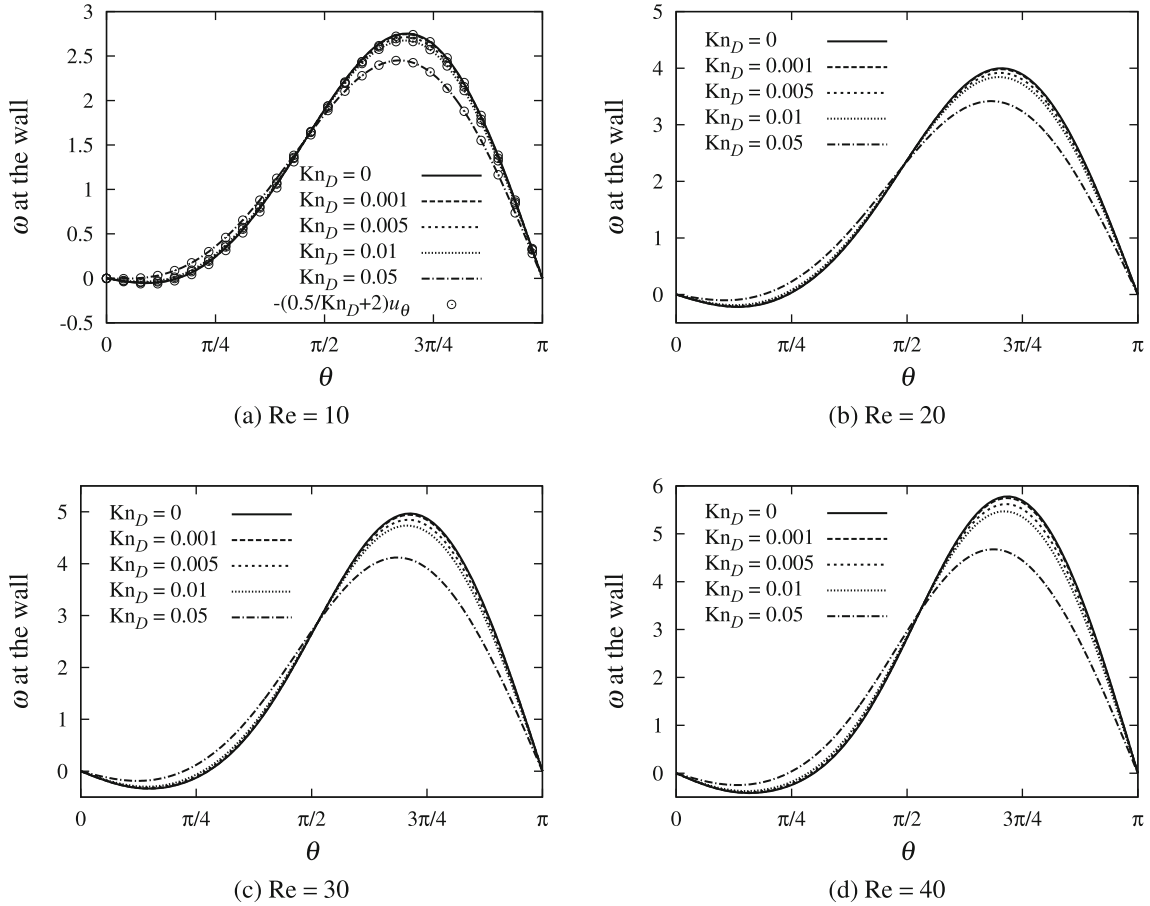


Fig. 11 Vorticity distribution along the wall for various Reynolds and Knudsen numbers in the steady flow regime

reviewed in the text, some papers did not present the formulation of the drag coefficient and only presented the results, some papers used the no-slip formula and some paper presented formulae for the slip case but did not validate them. Due to this controversy, we derived formulae for the various contributions to the drag coefficient and validated them by comparison to existing data, especially using an analytical solution of Oseen's equation for creeping flow around a cylinder with slip condition. At the end, some results are presented including wall vorticity and slip velocity distribution, streamlines, vorticity contours and various contributions to the drag coefficient.

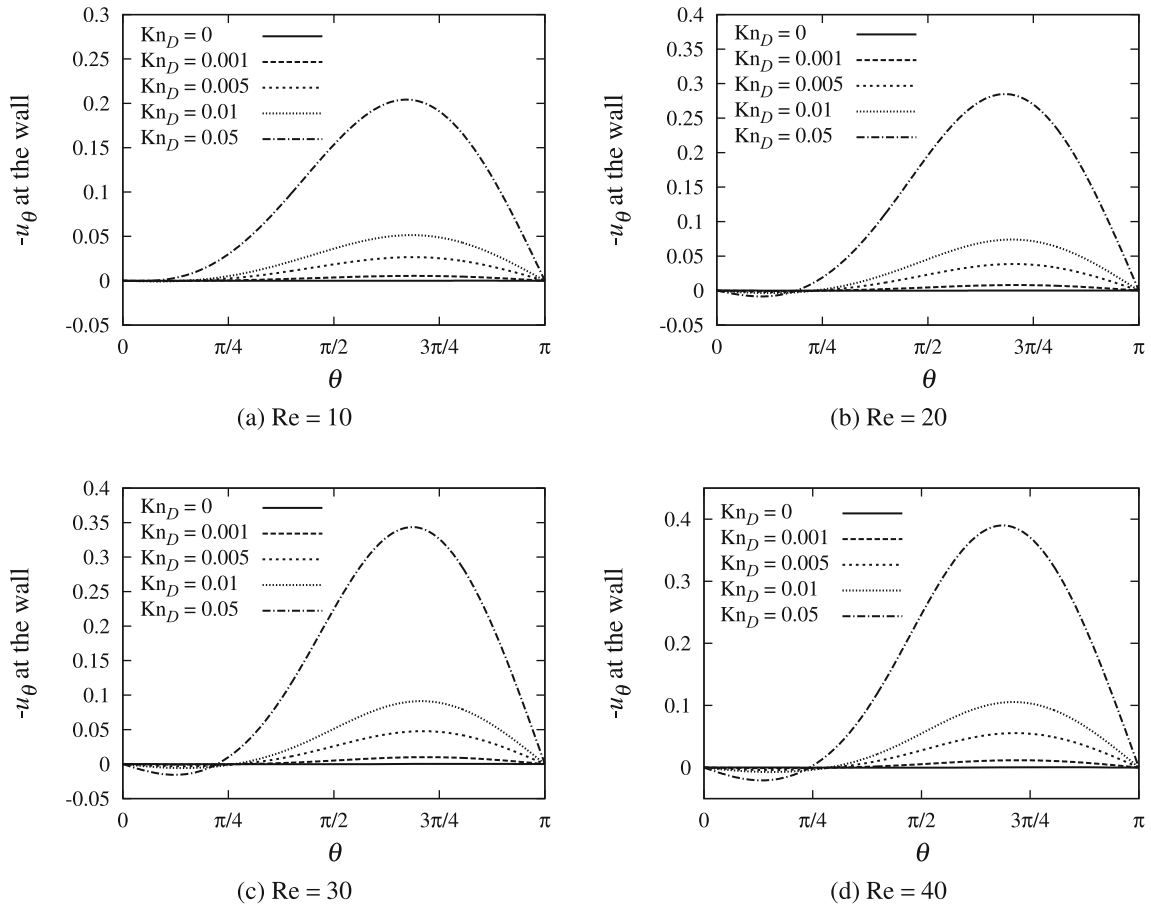


Fig. 12 Circumferential velocity distribution along the wall for various Reynolds and Knudsen numbers in the steady flow regime

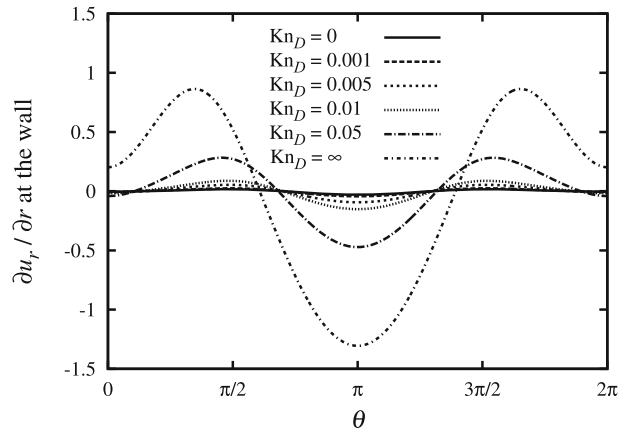


Fig. 13 The value of $\partial u_\theta / \partial r$ at the wall as a function of the circumferential angle θ at $Re = 20$ for $Kn = 0, 0.001, 0.005, 0.01, 0.05$ and ∞

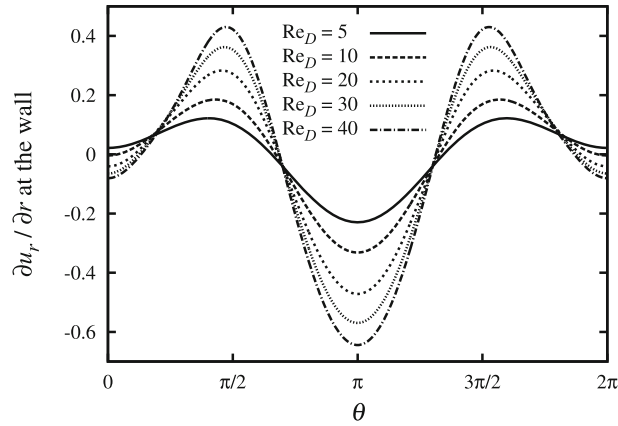


Fig. 14 The value of $\partial u_r / \partial r$ at the wall as a function of the circumferential angle θ at $\text{Kn} = 0.05$ for $\text{Re} = 5, 10, 20, 30$ and 40

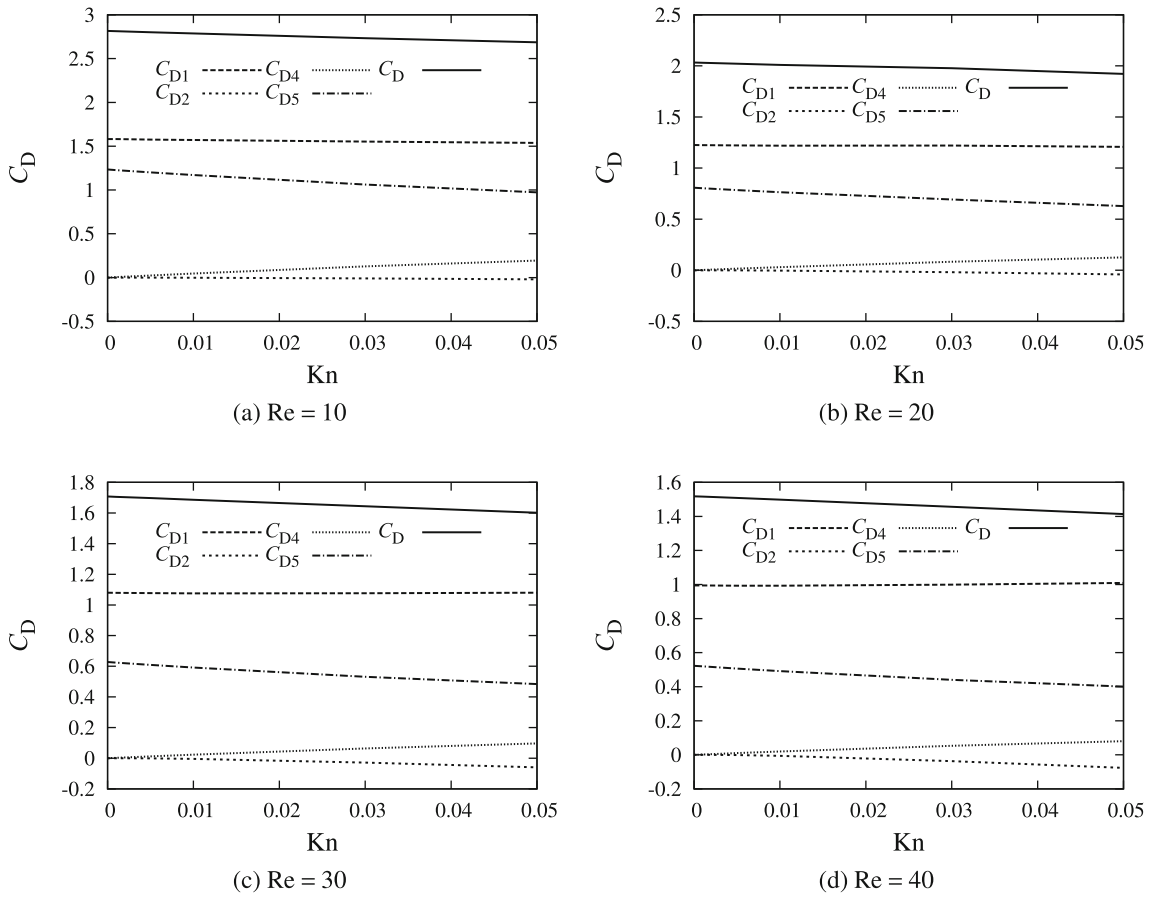


Fig. 15 Various contributions to drag coefficient and total C_D versus Knudsen number at $\text{Re} = 10, 20, 30$ and 40

Funding No funding was received for conducting this study.

Declarations

Conflict of interest The authors have no relevant financial or non-financial interests to disclose.

A Pressure distribution on the cylinder surface

In order to derive a general expression for the pressure distribution on the wall of a cylinder with velocity slip, which is required to calculate the drag and lift coefficients, we start from the non-dimensional θ -component of Navier–Stokes equation:

$$\frac{\partial u_\theta}{\partial t} + u_r \frac{\partial u_\theta}{\partial r} + \frac{u_\theta}{r} \frac{\partial u_\theta}{\partial \theta} + \frac{u_r u_\theta}{r} = -\frac{1}{r} \frac{\partial p}{\partial \theta} + \frac{2}{\text{Re}} \left(\frac{\partial^2 u_\theta}{\partial r^2} + \frac{1}{r} \frac{\partial u_\theta}{\partial r} - \frac{u_\theta}{r^2} + \frac{1}{r^2} \frac{\partial^2 u_\theta}{\partial \theta^2} \right). \quad (39)$$

On the cylinder wall, i.e. at $r = 1$, we identically have $u_r = 0$ and hence, Eq. (39) reduces to

$$\frac{\partial u_\theta}{\partial t} + \frac{u_\theta}{r} \frac{\partial u_\theta}{\partial \theta} = -\frac{1}{r} \frac{\partial p}{\partial \theta} + \frac{2}{\text{Re}} \left(\frac{\partial^2 u_\theta}{\partial r^2} + \frac{1}{r} \frac{\partial u_\theta}{\partial r} - \frac{u_\theta}{r^2} + \frac{1}{r^2} \frac{\partial^2 u_\theta}{\partial \theta^2} \right). \quad (40)$$

By differentiating the definition of vorticity (4) with respect to r , it is easy to show that at $r = 1$ we have

$$\frac{\partial \omega}{\partial r} = \frac{\partial^2 u_\theta}{\partial r^2} + \frac{1}{r} \frac{\partial u_\theta}{\partial r} - \frac{u_\theta}{r^2}. \quad (41)$$

By differentiating the incompressible continuity equation in cylindrical coordinates with respect to θ , it is straightforward to show that $\partial^2 u_\theta / \partial \theta^2$ vanishes at $r = 1$. From the slip boundary condition, one can deduce that the following relation holds:

$$u_\theta^2|_{r=1} = \frac{\omega^2|_{r=1}}{(\alpha + 1)^2}, \quad (42)$$

which leads to

$$\left[u_\theta \frac{\partial u_\theta}{\partial \theta} = \frac{1}{2} \frac{\partial (u_\theta^2)}{\partial \theta} = \frac{1}{2(\alpha + 1)^2} \frac{\partial (\omega^2)}{\partial \theta} \right]_{r=1}, \quad (43)$$

Supplying Eqs. (41), (42) and (43) to Eq. (40) gives

$$\frac{\partial p}{\partial \theta} \Big|_{r=1} = \left[\frac{2}{\text{Re}} \frac{\partial \omega}{\partial r} - \frac{1}{2(\alpha + 1)^2} \frac{\partial \omega^2}{\partial \theta} - \frac{\partial u_\theta}{\partial t} \right]_{r=1}. \quad (44)$$

The integration of Eq. (44) yields the following pressure distribution on the cylinder wall p_w as a function of θ and t :

$$p_w(\theta, t) - p_w(0, t) = \frac{2}{\text{Re}} \int_0^\theta \frac{\partial \omega}{\partial r} \Big|_{r=1} d\tilde{\theta} - \frac{1}{2(\alpha + 1)^2} [\omega^2|_{r=1}]_0^\theta - \int_0^\theta \frac{\partial u_\theta}{\partial t} \Big|_{r=1} d\tilde{\theta}. \quad (45)$$

Equation (45) is the same as the formulation provided by [21], whose proof is given in [22] using a conformal mapping from the Cartesian coordinate system, noting that the slip parameter β in D'Alessio's paper corresponds to $1/\alpha$ in the present work.

It is obvious that only the first term in the right-hand side (RHS) of Eq. (45) survives for the no-slip case as $\alpha \rightarrow \infty$. The second term in the RHS exists for a slip flow. The third term in the RHS holds for unsteady flows with slip.

References

1. Williamson, C.H.K.: Vortex dynamics in the cylinder wake. *Annu. Rev. Fluid Mech.* **28**, 477–539 (1996)
2. Manhart, M.: Vortex shedding from a hemisphere in a turbulent boundary layer. *Theoret. Comput. Fluid Dyn.* **12**, 1–28 (1998)
3. Breuer, M., Bernsdorf, J., Zeiser, T., Durst, F.: Accurate computations of the laminar flow past a square cylinder based on two different methods: Lattice-boltzmann and finite-volume. *Int. J. Heat Fluid Flow* **21**, 186–196 (2000)
4. Dennis, S.C.R., Chang, G.Z.: Numerical solutions for steady flow past a circular cylinder at Reynolds numbers up to 100. *J. Fluid Mech.* **42**, 471–489 (1970)
5. Fornberg, B.: A numerical study of steady viscous flow past a circular cylinder. *J. Fluid Mech.* **98**, 819–855 (1980)
6. D'Alessio, S.J.D., Dennis, S.C.R.: A vorticity model for viscous flow past a cylinder. *Comput. Fluids* **23**, 279–293 (1994)

7. Aghdam, S.K., Ricco, P.: Laminar and turbulent flows over hydrophobic surfaces with shear-dependent slip length. *Phys. Fluids* **28**, 035109 (2016)
8. Rothstein, J.P.: Slip on superhydrophobic surfaces. *Annu. Rev. Fluid Mech.* **42**, 89–109 (2010)
9. Kennard, E.H.: *Kinetic Theory of Gases*. McGraw-Hill, New York (1938)
10. Thalakkottor, J.J., Mohseni, K.: Unified slip boundary condition for fluid flows. *Phys. Rev. E* **94**, 023113 (2016)
11. Martin, M.J., Boyd, D.: Momentum and heat transfer in a laminar boundary layer with slip flow. *AIAA J. Thermophys. Heat Transf.* **20**, 710–719 (2006)
12. Aziz, A.: Hydrodynamic and thermal slip flow boundary layers over a flat plate with constant heat flux boundary condition. *Commun. Nonlinear Sci. Numer. Simul.* **15**, 573–580 (2010)
13. Atefi, G.: Quer angeströmter drehender Zylinder bei kleinen Reynoldszahlen und bei Schlupf. *Arch. Appl. Mech.* **61**, 488–502 (1991)
14. Legendre, D., Lauga, E., Magnaudet, J.: Influence of slip on the dynamics of two-dimensional wakes. *J. Fluid Mech.* **633**, 437–447 (2009)
15. Leal, L.G.: Vorticity transport and wake structure for bluff bodies at finite Reynolds number. *Phys. Fluids A* **1**, 124–131 (1989)
16. Li, D., Li, S., Xue, Y., Yang, Y., Su, W., Xia, Z., Shi, Y., Lin, H., Duan, H.: The effect of slip distribution on flow past a circular cylinder. *J. Fluids Struct.* **51**, 211–224 (2014)
17. Proudman, I., Pearson, J.R.A.: Expansions at small Reynolds numbers for the flow past a sphere and a circular cylinder. *J. Fluid Mech.* **2**, 237–262 (1957)
18. Seo, I.W., Song, C.G.: Numerical simulation of laminar flow past a circular cylinder with slip conditions. *Int. J. Numer. Meth. Fluids* **68**, 1538–1560 (2012)
19. Maghsoudi, E., Martin, M.J., Devireddy, R.: Momentum and heat transfer in laminar slip flow over a cylinder. *AIAA J. Thermophys. Heat Transf.* **27**, 607–614 (2013)
20. Shukla, R.K., Arakeri, J.H.: Minimum power consumption for drag reduction on a circular cylinder by tangential surface motion. *J. Fluid Mech.* **715**, 597–641 (2013)
21. D'Alessio, S.J.D.: Flow past a slippery cylinder: part 1 - circular cylinder. *Acta Mech.* **229**, 3375–3392 (2018)
22. D'Alessio, S.J.D.: Flow past a slippery cylinder: part 2 - elliptic cylinder. *Acta Mech.* **229**, 3415–3436 (2018)
23. Rehman, N.M.A., Kumar, A., Shukla, R.K.: Influence of hydrodynamic slip on convective transport in flow past a circular cylinder. *Theoret. Comput. Fluid Dyn.* **31**, 251–280 (2017)
24. Moin, P.: *Fundamentals of Engineering Numerical Analysis*. Cambridge University Press, (2010)
25. Williamson, J.H.: Low-storage Runge–Kutta schemes. *J. Comput. Phys.* **35**, 48–56 (1980)
26. Sucker, D., Brauer, H.: Fluidodynamik bei quer angeströmten Zylindern. *Wärme- und Stoffübertragung* **8**, 149–158 (1975)
27. Sen, S., Mittal, S., Biswas, G.: Steady separated flow past a circular cylinder at low Reynolds numbers. *J. Fluid Mech.* **620**, 89–119 (2009)
28. Nieuwstadt, F., Keller, H.B.: Viscous flow past circular cylinders. *Comput. Fluids* **1**, 59–71 (1973)
29. Moosaie, A.: Correction to: G. Atefi, Quer angeströmter drehender Zylinder bei kleinen Reynoldszahlen und bei Schlupf. *Arch. Appl. Mech.* **92**, 3065–3066 (2022)
30. Kocabiyik, S.: Analysis of the modified Oseen equations using orthogonal function expansions. *Can. Appl. Math. Q.* **1**, 475–492 (1993)

Publisher's Note Springer Nature remains neutral with regard to jurisdictional claims in published maps and institutional affiliations.

Springer Nature or its licensor (e.g. a society or other partner) holds exclusive rights to this article under a publishing agreement with the author(s) or other rightsholder(s); author self-archiving of the accepted manuscript version of this article is solely governed by the terms of such publishing agreement and applicable law.